



In vitro assessment of plasma-sprayed reinforced hydroxyapatite coatings deposited on Ti6Al4V alloy for bio-implant applications

Jarnail Singh^{1,a)}, Sukhpal Singh Chatha¹, Hazoor Singh¹

¹Yadavindra Department of Engineering, Punjabi University Guru Kashi Campus, Talwandi Sabo, Punjab, India

^{a)}Address all correspondence to this author. e-mail: jarnailsolanki@gmail.com

Received: 9 December 2021; accepted: 28 March 2022; published online: 11 April 2022

This research presents the basic in vitro assessment of bare Ti6Al4V alloy, hydroxyapatite (HA), and calcium silicate (CS)-reinforced HA coatings. The weight percentage of CS reinforcement in HA was varied as the HA- $x\%$ CS ($x=0, 10, \text{ and } 20 \text{ wt } \%$). The phase compositions, coating's microstructure, chemical properties, microhardness, porosity, surface roughness, and in vitro studies were performed. The HA-10%CS and HA-20%CS coatings displayed the crack-free morphology, whereas microcracks were observed over the surface of pure HA coating. With the progressive increment of CS content in HA, crystallinity, surface roughness, porosity, microhardness, and Young's modulus for HA-10%CS and HA-20%CS coatings increased compared to pure HA coating. The HA-10%CS and HA-20%CS coatings were more conducive and displayed superior hemocompatibility than HA. The HA-10%CS and HA-20%CS coatings exhibited no adverse effects on the erythrocytes, and the hemolysis rate (HR) was within the domain of safe value ($< 5\%$) for implant materials. The findings of this study indicate that surface modification of Ti6Al4V alloy with HA-10%CS and HA-20%CS coatings is a promising approach to improve the performance for bio-implant applications.

Introduction

With the advancements in biomedical field, the major body systems such as skeletal, circulatory, or nervous systems can be replaced or repaired by bio-implants. The orthopedic implants are used to correct deformities in the skeletal system and help restore the function of body parts [1]. Titanium-based implants, especially Ti6Al4V alloy, are used for orthopedic implant applications due to their favorable mechanical properties [2–5]. However, bio-inertness is a problem for using Ti6Al4V alloy as bio-implant [6]. An effective way to solve this problem is to deposit bioactive coating over the Ti6Al4V surface. It effectively combines the high strength and toughness of Ti6Al4V alloy with the biological properties of the bioactive coating material [3].

Hydroxyapatite [HA: $\text{Ca}_{10}(\text{PO}_4)_6(\text{OH})_2$] is known for its superior biocompatibility and bioactivity [7, 8]. The Ca/P ratio for HA is ~ 1.67 , which is similar to the bones and hard tissues [9]. These properties make HA an ideal coating material for various applications. The Atmospheric plasma spray (APS) is the most commonly used technique to deposit HA coating

over the metallic implants [10–15]. APS is known for its high deposition rate and low cost. The APS process is capable of high deposition in a short time along with a varied range of thickness. Moreover, the plasma spray coatings are advantages of high adherence with the substrate. The APS is a clinically approved technique to deposit HA by the Food & Drug Administration (FDA), USA [16]

Unfortunately, the poor mechanical properties of HA cause the premature failure of an implant in the presence of a local biological and mechanical environment [17]. It has been reported that introducing secondary phases in HA matrix improves its mechanical properties without sacrificing its biocompatibility [6, 18]. Recently, there have been numerous secondary reinforced phases has been introduced such as TiO_2 [19], SiO_2 [20], alumina [21], Silver [22], tantalum [23], Zinc oxide [6], niobium [24, 25], and carbon nanotubes [26].

Calcium silicate [CS, CaSiO_3] has been proposed as a potential material for bone tissue regeneration since it has been proved to be bioactive and degradable [27, 28]. Numerous

studies reported that the apatite formation rate of CS is higher than the other bioactive glasses and glass-ceramics [29–31]. The apatite forms on the surface of CS in a similar way as it does on the surface of CaO–SiO₂-based glasses. The dissolution of calcium ions increases the ion activity product of the apatite solution in the SBF from the CS, and apatite nucleation is facilitated by the hydrated silica on the surface of the CS. As a result, apatite nuclei grow quickly and spontaneously by consuming calcium and phosphate ions from the SBF solution [30–33]. Unfortunately, CS cannot be used in bulk form due to its higher degradation rate. The high degradation rate can increase the pH value of the surrounding environment and disturbances in cell vitality, which may limit the clinical application of CS-coated implants [34]. Alternately, using CS as a reinforcement filler in a composite system can be considered a good approach [35].

The recent reports on the HA–CS composite system have attracted significant attention. Beheri et al. [36] reported that mechanical properties were enhanced with increasing the CS content in the HA–CS composite. Lin et al. [37] fabricated the HA–CS composite with the different weight ratios and reported that with the increase of the CS content in HA–CS composite, the proliferation rate of the bone marrow mesenchymal stem cells (MSC) was increased. Similarly, other studies [38–45] also reported the results of the HA–CS composites.

Finally, it may be concluded that in the earlier investigation, HA–CS composites are well documented in the bulk form, but the studies based on the HA–CS composite coatings are minimal. As per the literature and best of the author's knowledge, there is no study available that reported the modification of Ti6Al4V alloy with composite HA–CS coating using atmospheric plasma spray (APS) process, which is the novelty of present research work. This research gap attracts the interest of authors to investigate the modification of Ti6Al4V alloy by depositing a composite coating of HA–CS through APS. In the present study, the 10 wt% and 20 wt% of CS mixed with HA are deposited on Ti6Al4V alloy with the APS process. The HA–CS coatings' surface characteristics, phase analysis, microhardness, elastic modulus, and biological performance are examined and compared with HA coating.

Results and discussion

Microstructural characterizations and composition analysis

Figure 1 shows the surface morphologies of HA, HA–10%CS, and HA–20%CS coatings. The coatings present the typical plasma-sprayed features such as irregularly shaped splats, pores, and partially melted particles. Also, fine nodular and sphere particles, which are adhered to fully melted splats, are the dominant surface features. During the plasma spray process, the powders were melted by the high temperature of the

plasma jet and deposited on the substrate surface at high speed, and smaller droplets were splashed out. The microstructure of the HA coating is a typical characteristic of the spreading of the molten droplets [10]. The size of the solidified particles and pore sizes for HA coating varies in the range of 1–10 μm and 3–8 μm, respectively. The measured size of spherical solidified particles and pore sizes for HA–10%CS varies in the range of 2–12 μm and 3–9 μm respectively, while for HA–20%CS coating particle size and pore sizes they varied in the range of 2–14 μm and 3–11 μm.

Both smooth areas and rough areas were present on the coating surface. The smooth and rough surfaces correspond to fully melted and partially melted particles. The HA–10%CS and HA–20%CS coatings [Fig. 1 (b, c)] exhibited the crack-free morphology, whereas microcrack can be observed over the surface of the HA coating [Fig. 1 (a)]. The solidification process of pure HA coating involves the single phase with homogeneous thermal conductivity resulting in a fast cooling rate, and a rapid cooling rate often results in microsurface cracks. In HA–10%CS and HA–20%CS coatings, the thermal gradient has been generated across the HA/CS boundary due to dissimilar thermal conductivities of HA and CS, which might be slower than the cooling rate of coatings. These findings are supported by the earlier studies of reinforced plasma-sprayed HA coatings, which also reported a thermal gradient due to dissimilar thermal conductivities of HA and reinforcement [24, 46]. Hence, HA–10%CS and HA–20%CS coatings displayed a crack-free morphology.

The chemistry spectrum was checked at various areas on the surface of HA–10%CS and HA–20%CS coatings [Fig. 1(a–c)]. The primary elements present on the surface of HA coating are Ca, P, and O, while Ca, P, O, and Si were found on HA–10%CS and HA–20%CS coatings. The calcium–phosphorus ratios (Ca/P) for HA coating at regions D, E, F, and G are 1.67, 1.67, 1.40, and 1.67, respectively. The Ca/P ratios for HA–10%CS coating at regions H, I, J, and K are 1.68, 1.74, 1.40, and 1.70, respectively, while Ca/P ratios for HA–20%CS at regions L, M, N, and O were 1.70, 1.40, 1.70, and 1.69, respectively. At areas D, E, G, H, I, K, L, N, and O, potential phases can be HA or the TTCP. In contrast, regions F, J, and M can be α-TCP or β-TCP [47]. The EDS analysis indicates that silicon is consistently distributed over the surface of the HA–10%CS and HA–20%CS coatings.

Surface roughness

Surface roughness has a significant impact on the implant characteristics. Surface roughness significantly affects the long-term in vivo response of the implant since the area of the implant in contact with the bone is increased with the rise in surface roughness [41]. The surface roughness facilitates cell adhesion, growth, and subsequent bone formation, promoting bio-integration

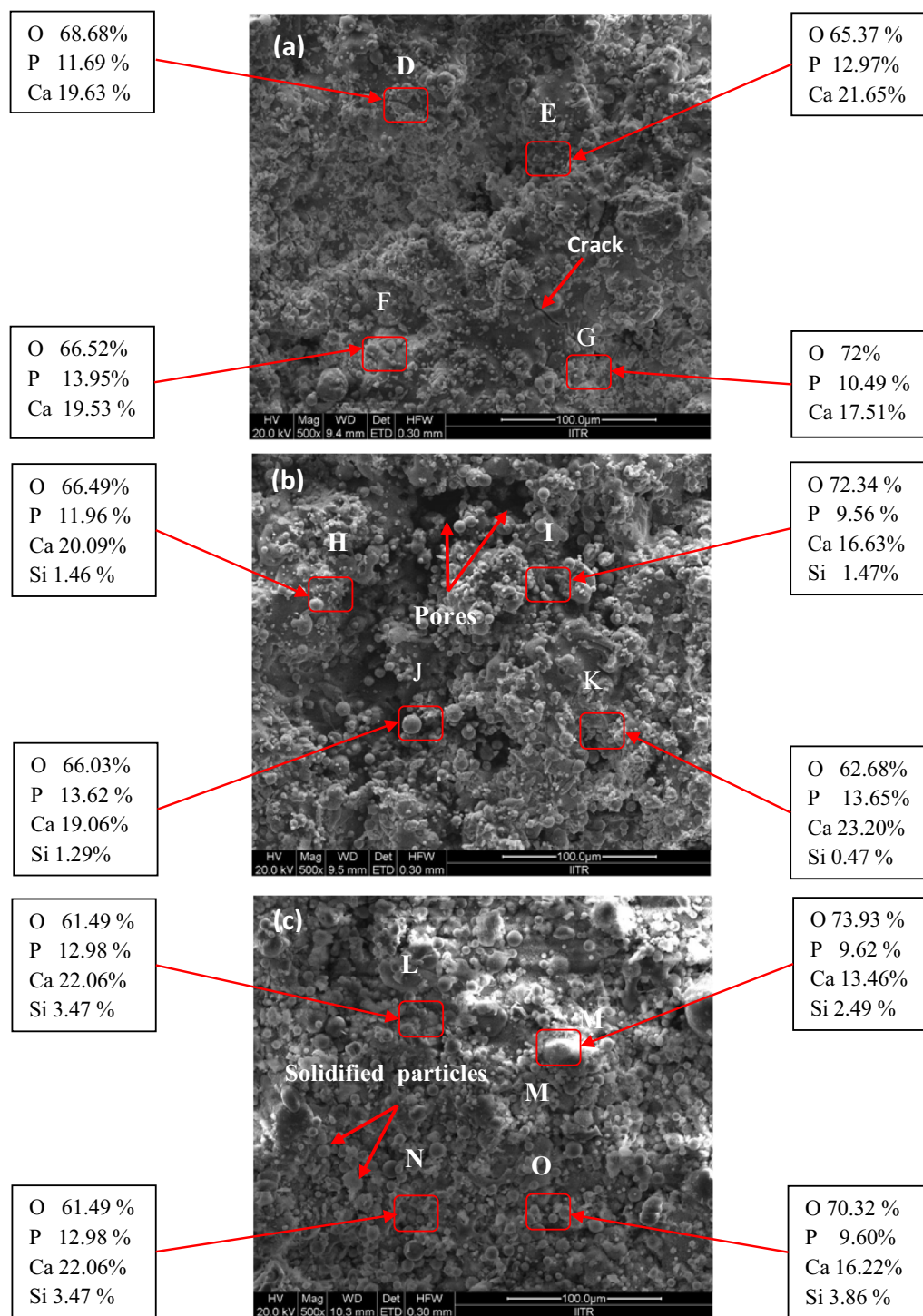


Figure 1: SEM Micrograph with EDS analysis showing elemental composition (wt%) at selected areas: (a) HA coating, (b) HA-10%CS coating, and (c) HA-20%CS coating.

and sturdiness to an implant [39]. Table 1 summarizes the surface roughness of HA, HA-10%CS, and HA-20%CS. The surface roughness of HA, HA-10%CS, HA-20%CS coatings is found to be $7.08 \pm 1.09 \mu\text{m}$, $8.48 \pm 1.97 \mu\text{m}$, and $9.46 \pm 1.27 \mu\text{m}$,

respectively. Although the HA-10%CS coating has a higher average surface roughness than the HA coating, there was no statistically significant difference ($P > 0.05$). However, the surface roughness of the HA-20%CS coating was significantly higher

TABLE 1: Summary of characteristics of HA, HA–10%CS, and HA–20%CS coatings.

S. No.	Sample Id	Surface roughness (μm)	Microhardness (HV)	Young's modulus (GPa)
1	HA	7.08 ± 1.09	194.64 ± 41.89	86 ± 4
2	HA + 10%CS	8.48 ± 1.97	224.78 ± 36.74	91 ± 5
3	HA + 20%CS	9.46 ± 1.24	238.75 ± 40.78	94 ± 2

($P < 0.05$) than that of the HA coating. The surface roughness results corroborate the uneven topography displayed by the coatings during the surface and cross-sectional analysis. It can be deduced from the surface roughness results that with the increase in the CS content in HA, the values of the surface roughness increase.

Cross-sectional hardness and Young's modulus

During implantation, the implant surface interacts with the complex physiological environment. It should have sufficient mechanical integrity in addition to having favorable biological properties [46]. Thus, hardness is important for good wear resistance and long service life [48]. The microhardness of HA, HA–10%CS, and HA–20%CS coatings is listed in Table 1. The microhardness of HA, HA–10%CS, and HA–20%CS coatings is 194.64 ± 41.89 , 224.78 ± 36.74 , and 238.75 ± 40.78 , respectively. The HA–10%CS and HA–20%CS coatings demonstrated significantly higher ($p < 0.05$) microhardness than HA. The hardness of the coatings is increased with the progressive increment of CS content in HA. The present study's microhardness lies well in the reported range of the previous study [36], i.e., 200–440 HV.

The Young modulus of the HA, HA–10%CS, and HA–20%CS coatings is shown in Table 1. The Young's modulus of HA (86 ± 4 GPa) is lower than HA–10%CS (91 ± 5 GPa) and HA–20%CS (94 ± 2 GPa), respectively. It is observed that Young's modulus increased gradually with the progressive increment of CS in HA.

Phase analysis

The X-ray diffraction of the starting powders is shown in Fig. 2. The well-defined sharp peaks of HA evidence the crystalline nature of the feedstock. The peaks corresponding to CS are noticed in HA–10%CS and HA–20%CS feedstock. It is worth noting that the peak intensity of CS peaks strengthens with the addition of CS in HA. Moreover, the feedstock is free from any impurities and amorphous phases. No shift in peak position was noticed after blending the CS powder with HA.

Figure 3 shows the diffractograms of the HA, HA–10%CS, and HA–20%CS coatings. It is observed that the diffractions peaks of coatings (Fig. 2) are broader than the corresponding peaks of the feedstock powder (Fig. 3). The broadening of the peaks is attributed to the reduction in the crystalline size [24]. In the present study, the crystallite size observed for as-sprayed

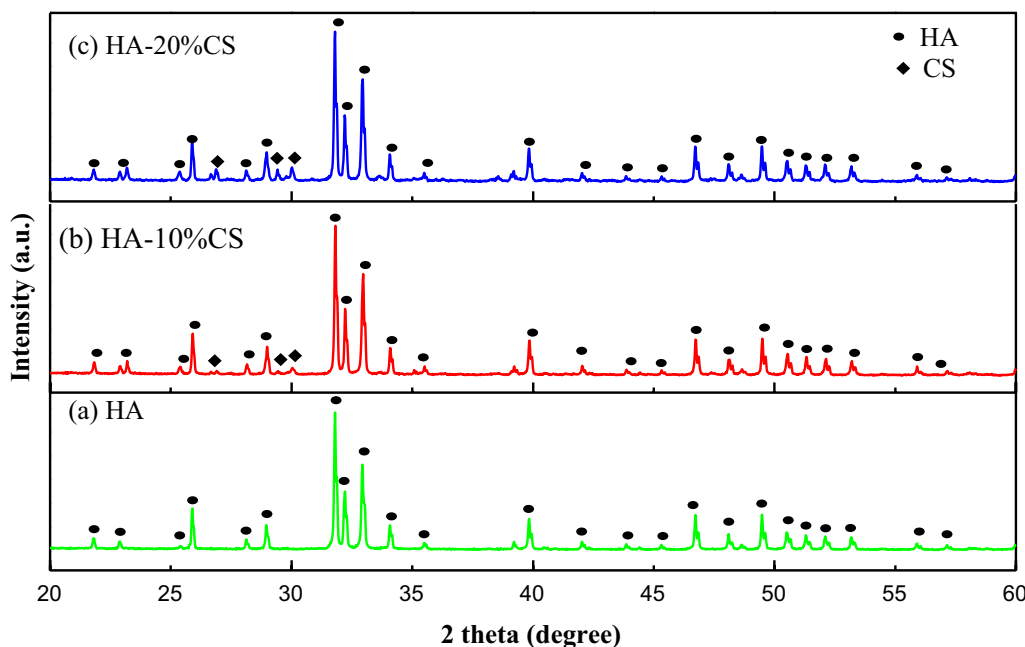


Figure 2: XRD diffractogram of (a) HA, (b) HA–10%CS, and (c) HA–20%CS feedstock powders.

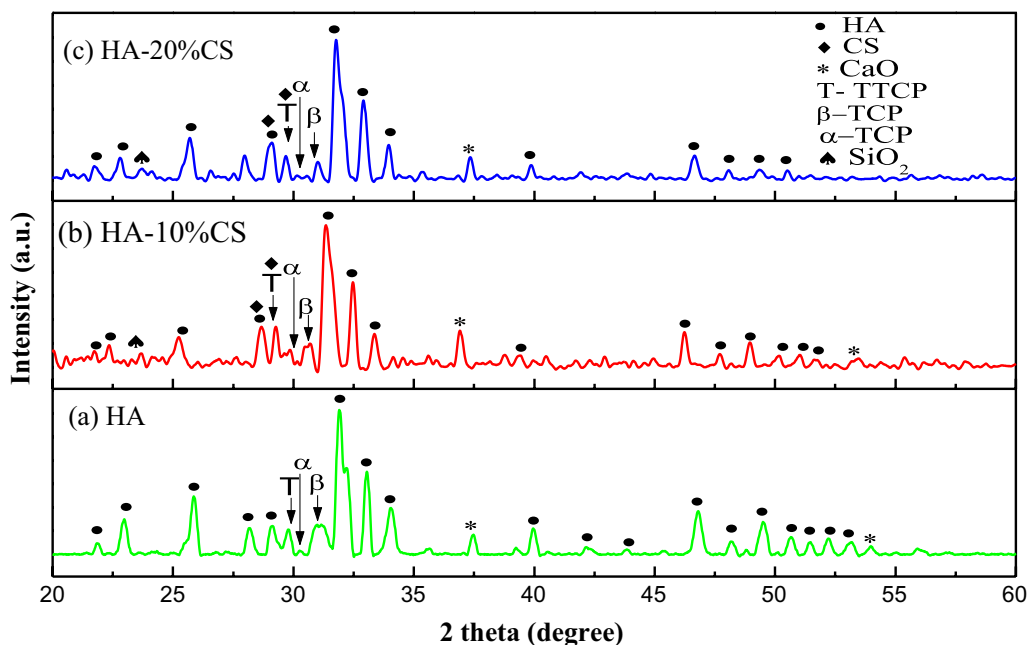


Figure 3: XRD diffractogram of the as-sprayed (a) HA, (b) HA-10%CS, (c) HA-20%CS coatings.

coatings was 4.3 ± 1 nm, while the crystallite size of feedstock powders was 8.3 ± 1 nm.

The primary phase present in the coatings is HA. Besides HA, the other phases identified in the coatings are α -tricalcium phosphate (α -TCP), β -tricalcium phosphate (β -TCP), and tetracalcium phosphate (TTCP). The amorphous phases such as α -TCP, β -TCP, and TTCP are present due to the decomposition of the HA powder in the high temperature of the plasma spray process [49]. In addition, wollastonite (CaSiO_3), CaO, and tridymite (SiO_2) phases were found in HA-10%CS and HA-20%CS coatings. The high temperature of the plasma spray process decomposes CS into tridymite (SiO_2) and calcium oxide (CaO). These results are consistent with the previous studies [29, 50, 51].

The HA, HA-10%CS, and HA-20%CS coatings have crystallinities of 76.75%, 77.34%, and 79.81%, respectively. The addition of CS in HA increases the coating crystallinity, implying that secondary phases like CaO, TCP, TTCP, and others are reduced. The higher crystallinity of the coating indicates better mechanical and biocompatibility properties [52]. It implies that CS reinforced in HA can improve the mechanical and biocompatibility properties.

Cytocompatibility

MTS assay

In the biological evaluation process, the cytotoxicity test is a preliminary test. The MTT assay was performed to evaluate the cytotoxicity of the substrate, HA, HA-10%CS, and

HA-20%CS coatings against the human bone osteosarcoma cells. The various samples' cell proliferation (MTS) data are depicted in Fig. 4, in which asterisk (*) denotes significance, i.e., P value < 0.05 . The proliferation of Ti6Al4V substrate, HA, HA-10%CS, and HA-20%CS coatings are 0.71 ± 0.009 , 0.86 ± 0.013 , 0.91 ± 0.014 , and 0.93 ± 0.013 , respectively. The Ti6Al4V alloy ($P < 0.05$) shows the least ability to promote cell growth. The HA-20%CS and HA-10%CS coatings show higher cell proliferation aptitude than HA coating, but no statistically significant difference ($P > 0.05$). These findings show that the HA-20% CS and HA-10% CS coating surfaces are more conducive to cell growth than the HA coating surface. The findings show that

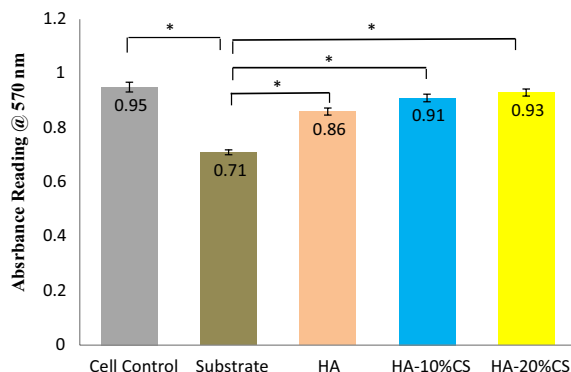


Figure 4: MTS assay for the viability of osteoblasts cultured on the substrate, HA, HA-10%CS, and HA-20%CS coatings (Data are presented as means \pm standard deviation, $n=3$, one-way ANOVA, $*P < 0.05$).

the ability of cells to proliferate improves as the content of CS in HA increases. The cell's health after the incubation with various samples is illustrated in Fig. 5. It is observed that the morphology of the cells was not affected after incubation with coated samples, indicating that the coatings do not have a cytotoxic effect.

Since the attachment of cells to implant surface can be influenced by topographical variation, the topography of the coated samples was determined by SEM. SEM images presented in Fig. 6 show the morphological features of MG-63 cells cultured on HA, HA-10%CS, and HA-20%CS coatings for 24 h. The cells were observed to adhere and spread, forming an intimate contact with the surface of coated specimens. Cell attachment was observed within 24 h of seeding on each surface studied, when seeded on the surface of coated samples. These features indicate that surface of coatings can promote the healthy development of osteoblast-like MG-63 cells. In the previous studies, such microstructures were favorable for enhancing greater mammalian cell adhesion and proliferation [19, 47]. Compared to HA coating, a higher number of cell growth and spreading of MG-63 cells over a wider surface area was seen on the HA-10%CS and HA-20%CS coatings. The surface morphology plays an important role in cell adhesion. Generally, the rough surface promotes a higher level of attachment than a smooth surface [45]. Therefore,

the surface topographical properties of HA-10%CS and HA-20%CS coatings helped increase the bone ingrowth and osseointegration process. Similarly, Beheri et al. also reported that HA-CS composites possessed good bioactivity and promoted cell growth [36].

Hemocompatibility

Hemocompatibility test is essential in assessing biomaterials, and it has long been the most widely used form of biocompatibility examination. When biomaterials corrode, ions leach into the blood system, raising the pH level and causing the membranes of red blood cells (RBCs) and erythrocytes to rupture. Hemolysis is caused by RBC rupturing, resulting in intercellular hemoglobin releasing. Thus, the hemolysis ratio (HR) is an important criterion for evaluating the hemocompatibility of biomaterials [24]. Figure 7 depicts the HR values for different samples, and the HR values (%) of Ti6Al4V, HA, HA-10%CS, and HA-20%CS are 4.82 ± 0.19 , 4.25 ± 0.21 , 3.88 ± 0.2 , and 3.17 ± 0.18 , respectively. The HR value of substrate and coatings was not significantly different. The HR values of uncoated Ti6Al4V alloy and coatings are lower than 5%, in the safe limit as described by ISO 10993-4 [46]. The quantitative analysis revealed that Ti6Al4V alloy demonstrated a higher HR value than the coated samples. The high HR value signifies increases in the local pH value of blood,

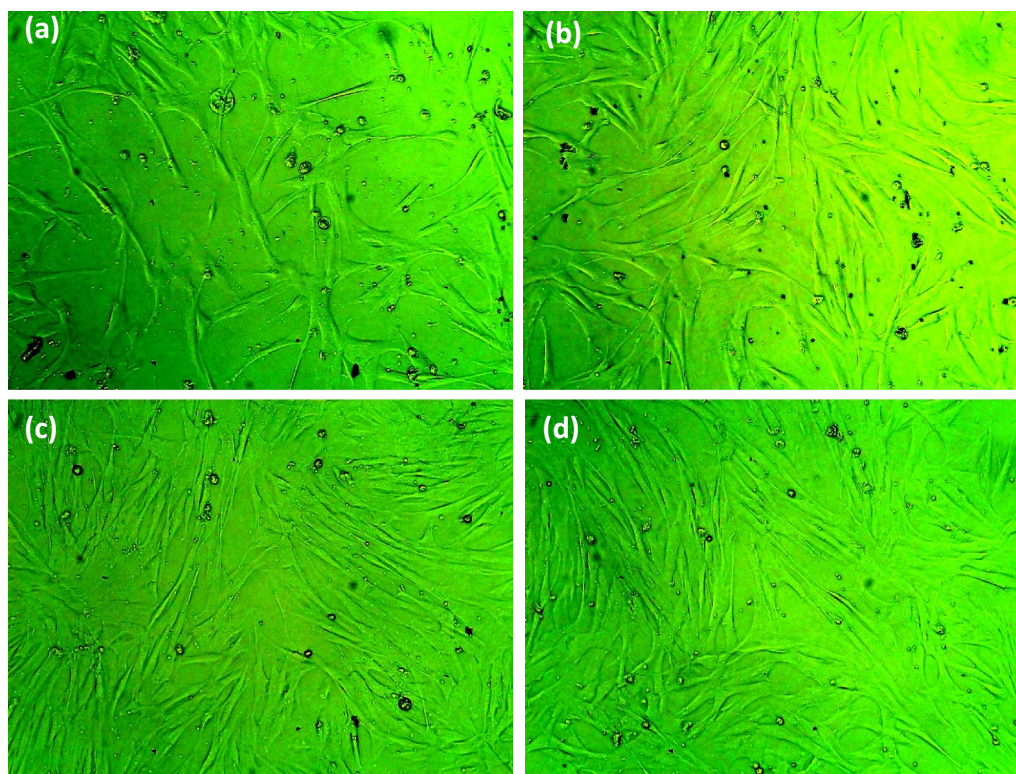


Figure 5: Cell health after incubation with (a) uncoated Ti6Al4V alloy, (b) HA, (c) HA-10%CS (d) HA-20%CS coating.

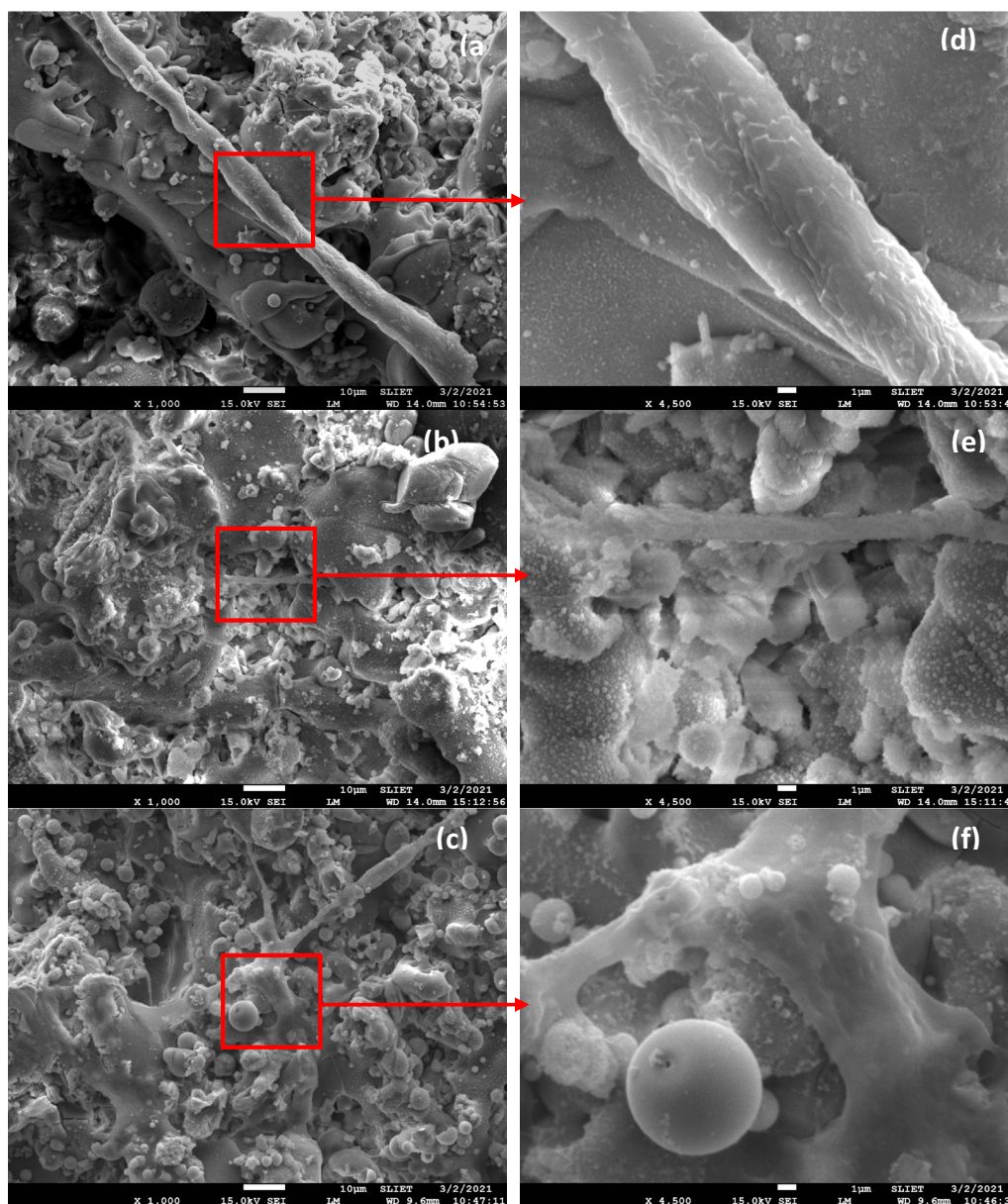


Figure 6: Adhesion and proliferation of MG-63 osteoblast-like cells during a 24-h incubation period; (a) HA coating (b) HA-10%CS coating (c) HA-20%CS coating. (d-f) high magnification view from the surface of (a-c). Representative SEM images show that MG-63 cells successfully colonized and proliferated on coatings surfaces.

resulting in RBC rupture. Higher hemolytic activity is linked to toxicity, and it can even inhibit cell growth. From the observation, both HA-10%CS and HA-20%CS coatings possessed lower HR values than HA. The progressive increment of CS in HA decreases the HR value. The findings of hemocompatibility analysis suggest that both HA-10%CS and HA-20%CS coatings can prevent the lysis of erythrocytes upon implantation. The cytotoxicity study indicated that the HA-10%CS and HA-20%CS coatings have non-cytotoxic properties and do not affect cell growth. Therefore, HA-10%CS and HA-20%CS coatings can be used for bio-implant applications.

Conclusions

The CS-reinforced HA coatings were successfully fabricated using atmospheric plasma spraying (APS) on Ti6Al4V alloy. Based upon the investigations in the present work, the following conclusions are drawn:

1. The coatings presented the typical plasma-sprayed features such as irregularly shaped splats, pores, and partially melted particles. The HA-10%CS and HA-20%CS coatings displayed crack-free morphologies, while microcracks were observed over HA coating.

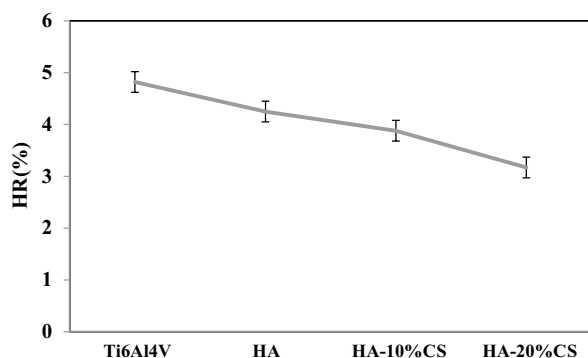


Figure 7: The HR value of the different samples.

- The HA, α -TCP, β -TCP, TTCP, and CaO phases were observed in HA coating. In addition, CaSiO_3 and SiO_2 phases were found in HA-10%CS and HA-20%CS coatings. The HA-10%CS and HA-20%CS coatings demonstrated better crystallinity than the pure HA coating, which indicates that fraction of amorphous phases decreased with the increase in CS content in the coatings.
- The HA-10%CS and HA-20%CS coatings exhibited higher surface roughness and Young's modulus than HA coating. Moreover, HA-10%CS and HA-20%CS coatings demonstrated significantly higher ($p < 0.05$) microhardness than HA coating. The findings showed that with the progressive increment of CS content in HA the mechanical properties are enhanced.
- The HA-10%CS and HA-20%CS coatings demonstrated superior cytocompatibility with higher cell proliferation of MG-63 cells, and the cell morphology appeared unaffected by CS addition. The HA-10%CS and HA-20%CS coatings displayed noticeable improvement in the hemocompatibility of Ti6Al4V alloy.
- A higher number of cell growth and spreading of MG-63 cells over a wider surface area was seen on the HA-10%CS and HA-20%CS coatings compared to HA coating.

The HA-CS composite coatings is a promising strategy to enhance the surface properties, cytocompatibility, and hemocompatibility of Ti6Al4V alloy. Since these studies are preliminary trials, more in-depth and extended in vitro and in vivo studies are required. The coatings deserve the optimization of CS content in HA to ascertain their usefulness for clinical applications.

Materials and methods

Feedstock powders for plasma-sprayed coatings

Clarion pharmaceutical Co., India supplied the HA powder, and CS powder was obtained from Wolkem, India limited. The starting size of the powder was $\sim 0.5 \mu\text{m}$. The feedstock material with

low mass to volume ratio could not flow freely in the spray gun. Hence to reduce inter-particle friction and improve flowability, the powders were mixed with the polyvinyl alcohol (PVA)-water solution to make a thick paste. The paste was dried at a temperature of 85°C in the oven and then particulate to pass through the sieves to obtain the required particle size. Figure 8(a) and (b) present SEM micrograph with EDS analysis of agglomerated HA and CS powders, respectively. The agglomerated powders have irregular morphology and blend small and large particles with an average particle size of $39 \pm 7 \mu\text{m}$. According to the EDS analysis, the Ca/P ratio for HA powder is well within the desired range of 1.67–1.76, whereas Ca/Si ratio for CS powder is 1. Three different compositions of powder agglomerates were prepared by varying the weight percentage of CS reinforcement in HA as HA- $x\%$ CS ($x=0, 10,$ and $20 \text{ wt}\%$) and classified as HA, HA-10%CS, and HA-20%CS.

Fabrication of plasma spray coating

The Ti6Al4V (ASTM F136) alloy was sectioned into thin plates had measurements of $15 \text{ mm} \times 10 \text{ mm} \times 2 \text{ mm}$. The specimens were grit blasted with alumina powder ($50\text{--}75 \mu\text{m}$) to enhance the mechanical bonding between the coating and the substrate. The average surface roughness of $5.95 \pm 1.23 \mu\text{m}$ was achieved after grit blasting. Furthermore, grit-blasted samples were exposed to compressed air to remove loose embedded alumina particles. The as-prepared feedstocks (HA, HA-10%CS, and HA-20%CS) were deposited on Ti6Al4V alloy. The coatings were deposited by atmospheric plasma spray (APS), and an F4 thermal spray gun carried out APS. An arc current of 500 amperes with 62 V of arc voltage was employed for plasma spraying. The primary and secondary carrier gases used are argon and hydrogen, with a flow rate of 38.1 SLPM and 6.48 SLPM, respectively. The stand-off distance (SOD) was kept at 90 mm.

Characterization of surface morphology, phase analysis, and surface properties

The surface morphology and composition examinations were executed by the Scanning Electron Microscope (SEM) (Merlin Compact, Carl Zeiss, Germany) equipped with an Energy-dispersive (EDS) detector. Before the cross-sectional examination, the surface was prepared. The specimens were cut along cross-section with a 120 r.p.m. slow-cutting precision saw, and then the samples were mounted in epoxy resin. Silicon carbide emery papers ranging from 220 to 3000 grit were used to polish the mounted specimens. The original powders and coating's phase analysis was conducted by X-ray diffraction (PANalytical, Almelo, The Netherlands) analysis with $\text{Cu K}\alpha$ radiation at 40 kV and 40 mA. The

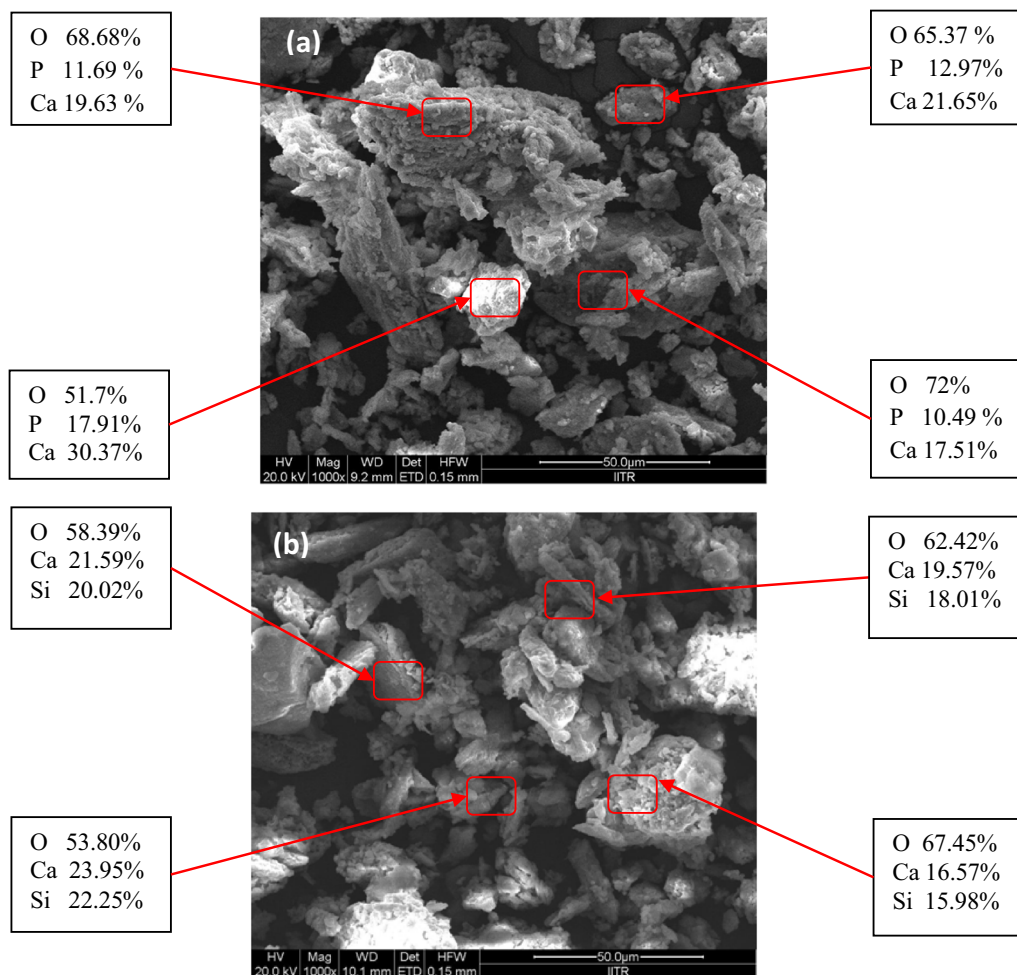


Figure 8: SEM Micrograph with EDS analysis showing elemental composition (wt. %) at selected areas: (a) HA powder (b) CS powder.

XRD spectra were acquired over a 2θ range of 20 to 60 °C at a scan rate of 0.05°/s. Phases and peaks were analyzed by X-pert high score plus software. The crystallinity of the coatings was measured by Rutland Method as described in an earlier study [53].

The microhardness tests were conducted on coating cross-sections using a Vickers microhardness tester (Mitutoyo HM-201) with a load of 1 N and a dwell time of 15 s. The surface roughness (Ra) was measured by portable surface roughness tester SJ-210 (Mitutoyo, Japan) with a 2 μm stylus diameter. Elastic modulus was determined using commercial nano-indentation equipment (MTS-G200).

In vitro cytocompatibility studies

The biocompatibility of the coatings was assessed with biological evolution. The human osteosarcoma MG-63 cell line (National Centre for Cell Science, Pune, India) was employed to investigate the cytotoxic behavior of the specimens. Gibco RPMI 1640 media

supplement with 10% (V/V) fetal bovine serum and 1% penicillin–streptomycin was used for cell culture. The specimens were sterilized by autoclaving before the cytotoxicity analysis. The cells were grown in a 12-well plate at 6000 cells/well seeded density for 96 h along with the specimens, and bare Ti6Al4V samples were treated as control. After 96 h incubation, specimens and media were extracted from the well plate. The cells were washed with Dulbecco's phosphate-buffered saline (DBPS) solution. Trypsinization of the cells was performed in the next phase, with 80 μl of 0.25% Trypsin–EDTA. Afterward, 96-well plate was used for seeding (100 μl/well) of the suspended cell. Finally, cytotoxicity of the samples was performed after 12-h incubation in the 96-well plate. BMG LABTECH microplate reader (CLARIOstar) was employed in determining the spectrophotometrical absorbance at 490 nm. The cell health was analyzed using the Thermo Fisher digital inverted microscope (EVOS XL).

A hemolysis test was conducted for the assessment of hemocompatibility. The blood sample for the hemolysis test was collected from a healthy adult volunteer and stored in heparinized

tubes. The centrifugation of the collected blood sample was done at 4 °C for 5 min at 2500 r.p.m, followed by the removal of supernatant to separate the RBCs. For the positive control, isotonic phosphate-buffered saline (pH 7.4) and for the negative control, Triton X100 were used to estimate the hemolysis. The uncoated and coated samples were incubated with 1% RBC suspension for five hours at 37 °C in a well plate. After the incubation, the suspension from the wells was collected in micro-centrifuge tubes and centrifuged at 2500 revolutions per minute (4 °C, 5 min). Finally, the measurement of the optical density of the supernatant was performed by a spectrophotometer at 540 nm wavelength. The value of the HR is calculated using the relation 1,

$$HR(\%) = \frac{DS - DN}{DP - DN} \times 100, \quad (1)$$

where DS is the absorbance of the coated/uncoated sample, DN and DP are the negative and positive control absorbance, respectively.

Statistical analysis

The average \pm standard deviation of ten measured values is reported in the present study. Significant differences were analyzed by one-way ANOVA, and the student's two-tailed *t*-test with a 95% confidence interval was performed for the statistical comparison (i.e., significant level with *P* value < 0.05) [46].

Acknowledgments

The authors gratefully acknowledge the financial support provided to this research by the University Grant Commission, New Delhi, India, under Grant Number RGNF-2013-14-SC-PUN-52049. The authors additionally thank Clarion pharmaceutical ltd., India and wolkem, ltd., India, for providing the HA and CS powders.

Data availability

The datasets generated during and/or analyzed during the current study are available from the corresponding author on reasonable request.

Declarations

Conflict of interest The authors declare that they have no known competing financial interest or personal relationships that could have influenced the work reported in this paper.

References

1. M. Talha, C.K. Behera, O.P. Sinha, A review on nickel-free nitrogen containing austenitic stainless steels for biomedical applications. *Mater. Sci. Eng. C* **33**, 3563–3575 (2013). <https://doi.org/10.1016/j.msec.2013.06.002>
2. G. Singh, T.R. Ablyaz, E.S. Shlykov, K.R. Muratov, A.S. Bhui, S.S. Sidhu, Enhancing corrosion and wear resistance of Ti6Al4V alloy using CNTs mixed electro-discharge process. *Micromachines* (2020). <https://doi.org/10.3390/M111090850>
3. A.S. Bhui, G. Singh, S.S. Sidhu, P.S. Bains, Experimental investigation of optimal ed machining parameters for Ti-6Al-4V biomaterial. *Facta Univ. Ser. Mech. Eng.* **16**, 337–345 (2018). <https://doi.org/10.22190/FUME180824033B>
4. G. Singh, S.S. Sidhu, P.S. Bains, M. Singh, A.S. Bhui, On surface modification of Ti alloy by electro discharge coating using hydroxyapatite powder mixed dielectric with graphite tool. *J. Bio- Tribo-Corros.* (2020). <https://doi.org/10.1007/s40735-020-00389-0>
5. R. Balokhonov, V. Romanova, A. Panin, S. Martynov, M. Kazachenok, Numerical study of stress-strain localization in the titanium surface modified by an electron beam treatment. *Facta Univ. Ser. Mech. Eng.* **14**, 329–334 (2016). <https://doi.org/10.22190/FUME1603329B>
6. R. Kumari, J. Dutta, Studies on corrosion resistance and bio-activity of plasma spray deposited hydroxylapatite (HA) based TiO₂ and ZrO₂ dispersed composite coatings on titanium alloy (Ti-6Al-4V) and the same after post spray heat treatment. *Appl. Surf. Sci.* **420**, 935–943 (2017). <https://doi.org/10.1016/j.apsusc.2017.05.208>
7. J. Singh, S.S. Chatha, H. Singh, Synthesis and characterization of plasma sprayed functional gradient bioceramic coating for medical implant applications. *Ceram. Int.* **47**, 9143–9155 (2021). <https://doi.org/10.1016/j.ceramint.2020.12.039>
8. J. Singh, S. Singh, H. Singh, Characterization and corrosion behavior of functional gradient hydroxyapatite coating. *J. Therm. Spray Technol.* (2018). <https://doi.org/10.1007/s11666-018-0802-3>
9. X. Zhang, W. Chaimayo, C. Yang, J. Yao, B.L. Miller, M.Z. Yates, Surface & coatings technology silver-hydroxyapatite composite coatings with enhanced antimicrobial activities through heat treatment. *Surf. Coat. Technol.* **325**, 39–45 (2017). <https://doi.org/10.1016/j.surfcoat.2017.06.013>
10. Y. Yang, Y. Wang, W. Tian, D. Ran Yan, J. Xin Zhang, L. Wang, Influence of composite powders' microstructure on the microstructure and properties of Al₂O₃-TiO₂ coatings fabricated by plasma spraying. *Mater. Design* **65**, 814–822 (2015). <https://doi.org/10.1016/j.matdes.2014.09.078>
11. V.F. Shamray, V.P. Sirotinkin, V.I. Kalita, V.S. Komlev, S.M. Barinov, A.Y. Fedotov, A.S. Gordeev, Study of the crystal structure of hydroxyapatite in plasma coating. *Surf. Coat. Technol.* **372**, 201–208 (2019). <https://doi.org/10.1016/j.surfcoat.2019.05.037>
12. E. Canas, M.J. Orts, A.R. Boccaccini, E. Sanchez, Microstructural and in vitro characterization of 45S5 bioactive glass coatings deposited by solution precursor plasma spraying (SPPS). *Surf.*

- Coat. Technol. **371**, 151–160 (2019). <https://doi.org/10.1016/j.surfcoat.2018.12.057>
13. S. Yang, H.C. Man, W. Xing, X. Zheng, Adhesion strength of plasma-sprayed hydroxyapatite coatings on laser gas-nitrided pure titanium. *Surf. Coat. Technol.* **203**, 3116–3122 (2009). <https://doi.org/10.1016/j.surfcoat.2009.03.034>
 14. X. Zhao, X. Liu, J. You, Z. Chen, C. Ding, Bioactivity and cytocompatibility of plasma-sprayed titania coating treated by sulfuric acid treatment. *Surf. Coat. Technol.* **202**, 3221–3226 (2008). <https://doi.org/10.1016/j.surfcoat.2007.11.026>
 15. V. Koshuro, A. Fomin, I. Rodionov, Composition, structure and mechanical properties of metal oxide coatings produced on titanium using plasma spraying and modified by micro-arc oxidation. *Ceram. Int.* **44**, 12593–12599 (2018). <https://doi.org/10.1016/j.ceramint.2018.04.056>
 16. A. Singh, G. Singh, V. Chawla, Characterization and mechanical behavior of reinforced hydroxyapatite coatings deposited by vacuum plasma spray on SS-316L alloy. *J. Mech. Behav. Biomed. Mater.* **79**, 273–282 (2018). <https://doi.org/10.1016/j.jmbbm.2018.01.005>
 17. R. Kumari, J. Dutta, Materials Characterization Microstructure and surface mechanical properties of plasma spray deposited and post spray heat treated hydroxyapatite (HA) based composite coating on titanium alloy (Ti-6Al-4V) substrate. *Mater. Charact.* **131**, 12–20 (2017). <https://doi.org/10.1016/j.matchar.2017.06.011>
 18. J. Singh, S. Singh, H. Singh, *Effect of Various Additives on Mechanical and Biological Properties of Hydroxyapatite Coating*, (2017), pp. 290–293
 19. S. Singh, C. Prakash, H. Singh, Deposition of HA–TiO₂ by plasma spray on β -phase Ti–35Nb–7Ta–5Zr alloy for hip stem: characterization, mechanical properties, corrosion, and in-vitro bioactivity. *Surf. Coat. Technol.* **398**, 126072 (2020). <https://doi.org/10.1016/j.surfcoat.2020.126072>
 20. G. Singh, H. Singh, B. Singh, Characterization and corrosion resistance of plasma sprayed HA and HA–SiO₂ coatings on Ti–6Al–4V. *Surf. Coat. Technol.* **228**, 242–247 (2013). <https://doi.org/10.1016/j.surfcoat.2013.04.036>
 21. M. Mittal, S.K. Nath, S. Prakash, Improvement in mechanical properties of plasma sprayed hydroxyapatite coatings by Al₂O₃ reinforcement. *Mater. Sci. Eng. C* **33**, 2838–2845 (2013). <https://doi.org/10.1016/j.msec.2013.03.005>
 22. M. Mirzaee, M. Vaezi, Y. Palizdar, Synthesis and characterization of silver doped hydroxyapatite nanocomposite coatings and evaluation of their antibacterial and corrosion resistance properties in simulated body fluid. *Mater. Sci. Eng. C* **69**, 675–684 (2016). <https://doi.org/10.1016/j.msec.2016.07.057>
 23. B. Singh, G. Singh, B.S. Sidhu, Analysis of corrosion behaviour and surface properties of plasma-sprayed composite coating of hydroxyapatite—tantalum on biodegradable Mg alloy ZK60. *J. Compos. Mater.* (2019). <https://doi.org/10.1177/0021998319839127>
 24. B. Singh, G. Singh, B. Singh, In vitro investigation of Nb–Ta alloy coating deposited on CoCr alloy for biomedical implants. *Surf. Coat. Technol.* **377**, 124932 (2019). <https://doi.org/10.1016/j.surfcoat.2019.124932>
 25. B. Singh, G. Singh, B.S. Sidhu, Investigation of the in vitro corrosion behavior and biocompatibility of niobium (Nb)–reinforced hydroxyapatite (HA) coating on CoCr alloy for medical implants. *J. Mater. Res.* **34**, 1–14 (2019). <https://doi.org/10.1557/jmr.2019.94>
 26. S. Liu, H. Li, Y. Su, Q. Guo, L. Zhang, Preparation and properties of in-situ growth of carbon nanotubes reinforced hydroxyapatite coating for carbon/carbon composites. *Mater. Sci. Eng. C* **70**, 805–811 (2017). <https://doi.org/10.1016/j.msec.2016.09.060>
 27. H. Chen, E. Zhang, K. Yang, Microstructure, corrosion properties and bio-compatibility of calcium zinc phosphate coating on pure iron for biomedical application. *Mater. Sci. Eng. C* **34**, 201–206 (2014). <https://doi.org/10.1016/j.msec.2013.09.010>
 28. H. Hu, Y. Qiao, F. Meng, X. Liu, C. Ding, Enhanced apatite-forming ability and cytocompatibility of porous and nanostructured TiO₂/CaSiO₃ coating on titanium. *Colloids Surf. B* **101**, 83–90 (2013). <https://doi.org/10.1016/j.colsurfb.2012.06.021>
 29. X. Liu, C. Ding, Characterization of plasma sprayed wollastonite powder and coatings. *Surf. Coat. Technol.* **153**, 173–177 (2002). [https://doi.org/10.1016/S0257-8972\(01\)01666-8](https://doi.org/10.1016/S0257-8972(01)01666-8)
 30. X. Liu, C. Ding, Z. Wang, Apatite formed on the surface of plasma-sprayed wollastonite coating immersed in simulated body fluid. *Biomaterials* **22**, 2007–2012 (2001). [https://doi.org/10.1016/S0142-9612\(00\)00386-0](https://doi.org/10.1016/S0142-9612(00)00386-0)
 31. W. Xue, X. Liu, X. Zheng, C. Ding, In vivo evaluation of plasma-sprayed wollastonite coating. *Biomaterials* **26**, 3455–3460 (2005). <https://doi.org/10.1016/j.biomaterials.2004.09.027>
 32. X. Liu, C. Ding, P.K. Chu, Mechanism of apatite formation on wollastonite coatings in simulated body fluids. *Biomaterials* **25**, 1755–1761 (2004). <https://doi.org/10.1016/j.biomaterials.2003.08.024>
 33. J. Singh, S.S. Chatha, H. Singh, Microstructural and in-vitro characteristics of functional calcium silicate topcoat on hydroxyapatite coating for bio-implant applications. *Prog. Biomater.* (2022). <https://doi.org/10.1007/s40204-022-00183-w>
 34. P. Tian, H. Hu, H. Wang, X. Liu, C. Ding, TiO₂/CaF₂ composite coating on titanium for biomedical application. *Mater. Lett.* **117**, 98–100 (2014). <https://doi.org/10.1016/j.matlet.2013.12.006>
 35. M. Yusuf, A. Bakar, N. Muhamad, M. Rafi, Incorporation of wollastonite bioactive ceramic with titanium for medical applications: an overview. *Mater. Sci. Eng. C* **97**, 884–895 (2019). <https://doi.org/10.1016/j.msec.2018.12.056>
 36. H.H. Beheri, K.R. Mohamed, G.T. El-bassyouni, Mechanical and microstructure of reinforced hydroxyapatite/calcium silicate nano-composites materials. *Mater. Des.* **44**, 461–468 (2013). <https://doi.org/10.1016/j.matdes.2012.08.020>

37. K. Lin, M. Zhang, W. Zhai, H. Qu, J. Changw, Fabrication and characterization of hydroxyapatite/wollastonite composite bioceramics with controllable properties for hard tissue repair. *J. Am. Ceram. Soc.* **105**, 99–105 (2011). <https://doi.org/10.1111/j.1551-2916.2010.04046.x>
38. A. Encinas-romero, S.R. Paya, Mechanical and bioactive behavior of hydroxyapatite—wollastonite sintered composites. *Int. J. Appl. Ceram. Technol.* **7**, 164–177 (2010). <https://doi.org/10.1111/j.1744-7402.2009.02377.x>
39. P. Feng, P. Wei, P. Li, C. Gao, C. Shuai, S. Peng, *Calcium silicate ceramic scaffolds toughened with hydroxyapatite whiskers for bone tissue engineering* (Elsevier, Amsterdam, 2014). <https://doi.org/10.1016/j.matchar.2014.08.017>
40. S. Kunjalukkal, F. Gervaso, M. Carrozzo, F. Scalerà, A. Sannino, A. Licciulli, Wollastonite/hydroxyapatite scaffolds with improved mechanical, bioactive and biodegradable properties for bone tissue engineering. *Ceram. Int.* **39**, 619–627 (2013). <https://doi.org/10.1016/j.ceramint.2012.06.073>
41. K. Lin, J. Chang, X. Liu, C. Ning, Synthesis and characterization of nanocomposite powders composed of hydroxyapatite nanoparticles and wollastonite nanowires. *Appl. Ceram. Technol.* **183**, 178–183 (2010). <https://doi.org/10.1111/j.1744-7402.2009.02474.x>
42. R. Morsy, R. Abuelkhair, T. Elnimr, A facile route to the synthesis of hydroxyapatite/wollastonite composite powders by a two-step. *Silicon* (2015). <https://doi.org/10.1007/s12633-015-9339-y>
43. A. Encinas-romero, S. Aguayo-salinas, F.F. Castillo, Synthesis and characterization of hydroxyapatite—wollastonite composite powders by sol–gel processing. *Appl. Ceram. Technol.* **5**, 401–411 (2008). <https://doi.org/10.1111/j.1744-7402.2008.02212.x>
44. A.P. Solonenko, A.I. Blesman, D.A. Polonyankin, Materials characterization poorly crystallized hydroxyapatite and calcium silicate hydrate composites: synthesis, characterization and soaking in simulated body fluid. *Mater. Charact.* **161**, 110158 (2020). <https://doi.org/10.1016/j.matchar.2020.110158>
45. Y. Huang, H. Zhang, H. Qiao, X. Nian, X. Zhang, Anticorrosive effects and in vitro cytocompatibility of calcium silicate/zinc-doped hydroxyapatite composite coatings on titanium. *Appl. Surf. Sci.* **357**, 1776–1784 (2015). <https://doi.org/10.1016/j.apsusc.2015.10.034>
46. B. Singh, G. Singh, B. Singh, N. Bhatia, In-vitro assessment of HA–Nb coating on Mg alloy ZK60 for biomedical applications. *Mater. Chem. Phys.* **231**, 138–149 (2019). <https://doi.org/10.1016/j.matchemphys.2019.04.037>
47. D.Q. Pham, C.C. Berndt, U. Gbureck, H. Zreiqat, V.K. Truong, A.S.M. Ang, Mechanical and chemical properties of Baghdadite coatings manufactured by atmospheric plasma spraying. *Surf. Coat. Technol.* **378**, 124945 (2019). <https://doi.org/10.1016/j.surfcoat.2019.124945>
48. X. Chen, B. Zhang, Y. Gong, P. Zhou, H. Li, Mechanical properties of nanodiamond-reinforced hydroxyapatite composite coatings deposited by suspension plasma spraying. *Appl. Surf. Sci.* **439**, 60–65 (2018). <https://doi.org/10.1016/j.apsusc.2018.01.014>
49. X. Liu, D. He, Z. Zhou, G. Wang, Z. Wang, X. Guo, Effect of post-heat treatment on the microstructure of micro-plasma sprayed hydroxyapatite coatings. *Surf. Coat. Technol.* **367**, 225–230 (2019). <https://doi.org/10.1016/j.surfcoat.2019.03.056>
50. X. Liu, C. Ding, Phase compositions and microstructure of plasma sprayed wollastonite coating. *Surf. Coat. Technol.* **141**, 269–274 (2001). [https://doi.org/10.1016/S0257-8972\(01\)01169-0](https://doi.org/10.1016/S0257-8972(01)01169-0)
51. W. Wang, J. Liang, X. Guo, F. Xuan, H. Hong, Mechanical properties and dissolution behavior of plasma sprayed wollastonite coatings deposited at different substrate temperatures. *J. Therm. Spray Technol.* **21**, 496–504 (2012). <https://doi.org/10.1007/s11666-011-9699-9>
52. S. Mohajernia, S. Pour-Ali, S. Hejazi, M. Saremi, A.R. Kiani-Rashid, Hydroxyapatite coating containing multi-walled carbon nanotubes on AZ31 magnesium: mechanical-electrochemical degradation in a physiological environment. *Ceram. Int.* **44**, 8297–8305 (2018). <https://doi.org/10.1016/j.ceramint.2018.02.015>
53. G. Singh, S. Singh, S. Prakash, Surface characterization of plasma sprayed pure and reinforced hydroxyapatite coating on Ti6Al4V alloy. *Surf. Coat. Technol.* **205**, 4814–4820 (2011). <https://doi.org/10.1016/j.surfcoat.2011.04.064>